Design and Integration of a Novel Spatial Articulated Robotic Tail

Wael Saab , William S. Rone Jr., Anil Kumar, *Member, IEEE*,
and Pinhas Ben-Tzvi , *Senior Member, IEEE*

Abstract—In nature, tails are a key feature in numerous animals that help stabilize, maneuver, manipulate, and/or propel. However, prior research on robotic tails has focused on limited degree of freedom (DOF), pendulum-like structures designed for a single function. This paper presents a novel robotic tail system capable of spatial motion to generate spatial loading. The roll–revolute–revolute robotic tail (R3RT) is a serpentine robotic structure with a roll-DOF at the tail base, and two independently actuated coplanar bending segments composed of several links connected by parallel revolute joints. A dynamic model of the tail is presented, along with considerations for sensing the robot's state and controlling the tail. The inertial loading capabilities of the tail are analyzed using the dynamics model and experimentally validated using an integrated prototype of the R3RT to present loading analysis and the performance benefits of tail articulation. Results of the analysis are promising and indicate clear directions for improvement in a future work.

Index Terms—Cable-driven, hyper-redundant robot, legged robot, mobile robot, robotic tail.

I. INTRODUCTION

IN NATURE, tails assist propulsion, stabilization, maneuvering, and manipulation. However, other than undulating or swimming snake robots, the focus has been on leg design and control to propel, maneuver, and stabilize. By offsetting some maneuvering and stabilization functions to a tail, the leg design and control complexity can be reduced.

The roll–revolute–revolute robotic tail (R3RT) is a spatial tail structure capable of generating spatial loading at its base. This paper treats the design, modeling, and implementation of the R3RT, with a future work planned for detailed task planning

and control. The R3RT is part of ongoing research studying articulated robotic tails capable of augmenting a legged robot's ability for agile and robust terrain traversal in unstructured environments [1], [2]. Beyond application as a tail, the R3RT design is also envisioned for use in a snake-like mobile robot, fish- or tentacle-like aquatic propulsion, energy harvesting by an articulated structure and satellite reorientation.

As for contribution, this is the first publication to focus on the R3RT's design, dynamics, and experimental results. In [1], a generalized serpentine structure was used to analyze quadrupedal maneuvering. In [3], the R3RT was utilized as a tail structure for a preliminary analysis of tail-based quadruped maneuvering/stabilization. This paper builds on [1] by experimentally verifying the dynamic analysis showing the benefits of articulated tail structures over pendulum structures. This paper expands on [3] by considering actuation-input-based tail commands instead of prescribed joint angles.

II. BACKGROUND AND DESIGN MOTIVATION

A. Inertial Adjustment Mechanisms—Prior Work

This section reviews inertial adjustment mechanisms that generate loading independent of ground contact. These mechanisms can be classified as follows: substrate interaction mechanisms (e.g., propellers and thrusters) that propel ambient fluid to produce force, translational mechanisms (e.g., a reaction mass) that generate reaction forces and adjust center-of-mass (COM) location [4], and rotational mechanisms, including symmetric systems (e.g., reaction wheels) with their COM along the rotation axis that generate reaction moments and asymmetrical systems (e.g., pendulums and robotic tails) that generate reaction forces and moments and/or move the COM.

Substrate interaction and translational mechanisms are not practical on legged robots due to size/weight requirements. Reaction wheels can have small envelopes and continuously rotate, but their performance is limited by mass constraints and the actuator speed [5]. Robotic tails require larger workspaces but benefit from larger moments of inertia due to the length over which mass is distributed. Comparative analysis between tails and reaction wheels has shown that tails are more appropriate when a high moment of inertia mechanism can be accommodated and timescales are short, whereas reaction wheels better perform when continuously rotated over long time scales [5]. Therefore, tails are best suited for aggressive inertial adjustment applications for mobile robotic systems [6].

TABLE I
COMPARISON OF ROBOTIC TAIL DESIGNS, ACTUATION PROPERTIES, AND ESTIMATED PEAK MOMENTS PROVIDED AT TAIL BASE

System	[16]	[8], [9]	[10]	[13]^A	[12]	[14]	[18]	[7]	[19]	**R3RT**
Tail Mass (g)	700	400	371	1000	17	4	70	400	150	900
Tail Length (mm)	150	500	177	500	103	115	73	500	300	500
Rated Motor Power (W)	5.5	120	19^B	-	4	2.5^B	1.75^B	70 ea.	426^B	100 ea.
Max. Speed (RPM)	6	275	240^B	21	3000	400^B	320^B	137	353^B	260
End-Effector Workspace (Deg)	180	224	220	-	255	265	135/135	180/70	180/180	270/∞
Mechanical Design	Planar						Spatial			
	Single-Body Rigid Pendulum									Articulated

^{A}Simulation.
^{B}Values from [6].

B. Existing Robotic Tail Designs

Robotic tails in the literature draw inspiration from animals such as cheetahs [7]–[9], kangaroos [10], fish [11], and lizards [12]. To compare prior tails to the R3RT, Table I summarizes a sample of the prior work. In terms of mechanical design, prior research has primarily focused on planar pendulums covering a wide range of masses (17–1000 g) and lengths (73–500 mm). Planar tails operate with 1-DOF in the pitch [8], [12], [13], yaw [11], [14]–[16], or roll [9] directions. The spatial tails are 2-DOF single-mass pendulums operating in multiple planes, like pitch–yaw [7], [17]–[20]. Planar tails provide enhanced performance about a single body-axis with advantageous simple design and control. Spatial tails greatly increase the workspace and provide multiaxis performance at the cost of increased design and control complexity.

Functionally, these tails aid propulsion, stabilization, or maneuverability. Propulsion use cases include swimming [11], assisting acceleration [8], and climbing [15]. Stabilization use cases include passive walking [16], maintaining constant attitude [17], disturbance rejection [20], and airborne attitude control [7], [10], [12], [13], [19]. Maneuvering use cases include yaw [14] and roll [9] turning.

Recent research has simulated the impact of robotic tails ranging from a single-body 1-DOF pendulum to an articulated 6-DOF tail on the yaw-angle maneuvering of a legged robot [1]. These simulations indicate that tail articulation enhances the yaw inertial loading compared to a pendulum-like tail. Furthermore, multisegment tails can execute multiple mode shapes, which enable greater COM position control (see Section VI-A) and enhanced inertial loading [21]. Implementation of increased articulation requires a more sophisticated mechanical design and additional actuators for controlled motion. To address these challenges, prior research on high-DOF articulated structures has been considered.

C. Existing Articulated Robotic Structures

This section reviews previous articulated robots to identify design challenges and highlight useful design criteria that inspired the R3RT design. The two main classes of high-DOF articulated robots are continuum and serpentine.

Continuum robots bend continuously along their length. Extrinsically actuated designs have a base actuation unit, an actuation transmission system (e.g., cables, rods), and an elastic backbone structure. Intrinsically actuated designs integrate actuation along the robot and generate motion by expanding/contracting these actuators. Although continuum robots can form articulated spatial curvatures, significant challenges remain in terms of modeling, sensing, and controlling these structures due to the absence of conventional joints, all of which are active areas of research [22], [23].

Serpentine robots comprise a serial chain of numerous rigid links and form discrete curvatures. Traditional serpentine robots are actuated at each joint, but this increases a robot's mass, size, and torque requirements. Another approach centralizes actuation and uses actuation cabling similar to extrinsic continuum robots with elastic elements regulating joint rotation [24]. This approach requires individual cable actuation since cable displacements are not generally equal during motion. Rolling contact joints with custom contours have been demonstrated to maintain equal antagonistic cable displacements and overcome the elastic elements' joint angle limits. These two cables may connect to a single driving pulley, which reduces the quantity of actuators [25], and multisegment curvature actuation can be decoupled using a hollow backbone for neutral axis cable routing [24].

The merits of extrinsic actuation in serpentine robots are widely demonstrated in robotic hand/finger/gripper designs with more joints than actuators to reduce manipulator size and inertia. Fixed motion coupling can distribute angles via gears [26], belts/pulleys [27], and linkages [28] that provide structural rigidity and accurate trajectory tracking. Cable transmission systems are also used to produce motion with angle distribution methods such as friction pulleys [29], higher order rolling pairs [30], and spring-loaded joints [31].

D. Design Motivation and Requirements

Three requirements drive the R3RT design. First, the R3RT should be spatial and multifunctional, capable of affecting the mobile robot dynamically and quasi-statically. Quasi-static loading uses the tail to modify the system's COM position; therefore, the R3RT should have a large workspace to maximize COM adjustments. Dynamic loading uses rapid tail motions to generate high-magnitude inertial loading to affect the system dynamics; a spatial R3RT should provide yaw, pitch, and roll loading. While the robot would not be able to apply an arbitrary loading profile, it should be capable of generating significant moments about all directions.

Second, the R3RT should be articulated and be capable of multiple mode shapes. Articulation enhances loading compared to that of a pendulum-like structure [1], [21], and serpentine
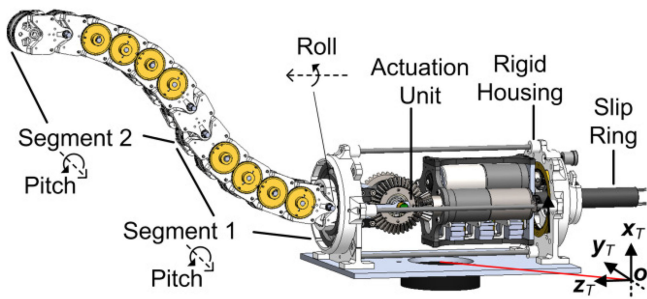
Fig. 1.   R3RT system design.

articulation is chosen for its conventional design, modeling, and sensing. Extrinsic actuation transmitted by cabling is chosen to reduce the minimum tail size, inertia, and actuator loads. Fixed motion coupling will constrain the links' relative motion within tail segments, and cables routed along contoured cylindrical links will decouple the tail segments' actuation and ensure equal and opposite antagonistic cable displacement.

Third, the R3RT must be designed to operate in a cantilevered mode. Several macroscale-articulated robots are designed for vertical operation without consideration for cantilevered mounting. The tail design should be capable of remaining fully extended with minimal to no actuation.

E. Design Innovations

Based on Section II-D design requirements, a novel spatial tail is proposed that provides the following innovations relative to robotic tails and serpentine robots in literature: novel implementation of a dexterous tail structure capable of forming two mechanically decoupled tail mode shapes, enhanced COM and end-effector workspaces due to the two independent tail segments (see Section VI-A), enhanced articulated tail inertial loading capabilities compared to pendulum-like tails (experimentally verified, see Section VII-C), and spatial tail curvatures enabled via an infinite roll rotation that can operate as both a symmetrical and an asymmetrical inertial adjustment mechanism (see Section VI-B).

III. MECHANICAL DESIGN

A. Rigid Housing and Actuation Unit

The R3RT mechanical design, shown in Fig. 1, consists of a rigid housing, an actuation unit, and tail segments. The rigid housing consists of two frames connected together with steel rods to provide a lightweight R3RT support structure. Two bearings set in the rigid housing provide the R3RT roll-DOF, an internal gear is mounted on the rigid housing to facilitate roll-DOF actuation, and an absolute encoder is mounted on the rigid housing and coupled to the actuation module via a timing belt. A high-current miniature slip ring (Orbex 300 Series) transmits control signals and motor current to the actuation unit. This allows the R3RT to continuously rotate; when the tail segment's COM aligns with the roll axis, the R3RT is a reaction wheel. This is an advantage over prior tail designs (see Table I) with more constrained workspaces (see Section VI-A).
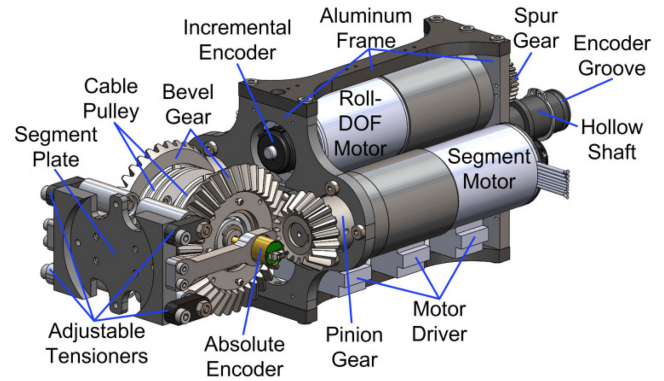

Fig. 2.   R3RT actuation module.

The tail actuation unit (see Fig. 2) consists of three gear motors: one for the roll-DOF and two for the tail segment DOFs. The roll-DOF motor attaches to a spur gear meshed with the rigid housing internal gear. Each segment gear motor couples with a two-channel pulley through a pinion/bevel gear reduction. The bevel-gear-mounted pulleys connect to the antagonistic cable pair that actuates the motor's tail segment. Four adjustable tensioning mechanisms with passive rollers individually tension the two antagonistic cables per actuated segment to ensure a straight home configuration and minimize backlash.

B. Tail Segments

Fig. 1 shows the tail segment design. Twelve bodies (links 1–12) are connected serially to create a two-segment robotic structure capable of planar "bending." Link 1 is connected to Link 0 through a revolute joint, which is rigidly attached to the actuation unit's segment plate (see Fig. 2).

The remaining 11 links are connected by revolute joints parallel to the Links 0/1 joint. Therefore, when the roll angle is ±90°, the tail remains extended without requiring actuation (meeting the Section II-C cantilevered-operation design requirement). Distinct segments are created by terminating pairs of antagonistic cables along the robot—in Fig. 1, two segments are created by terminating cables at Links 6 and 12.

The R3RT link design ensures equal antagonistic cable displacements by routing cables along nested cylindrical surfaces. Fig. 3(a) shows the cable paths for Segment 1, in which the cable pairs route along six cylindrical surfaces before terminating at Link 6. Segment 1 antagonistic cable displacements are defined by the linear relationship $\pm 6 r_{\mathrm{cbl}} \theta_i$, where r_{cbl} is the cylinder contour radius and θ_i is the relative link rotation. Since joint motions increase/decrease the cable path length by the same amount on opposite sides, a single pulley can control both cables.

The R3RT cable routing also mechanically decouples the Segment 1 and 2 actuation. Fig. 3(b) shows the cable paths for Segment 2. Within Segment 2, the cable routing is similar to the Segment 1 cables in Links 1–6 in Fig. 3(a). However, through Links 1–6, Segment 2 cabling routes along an S-path and crosses the R3RT between Links 2 and 3. With this S-path routing, the
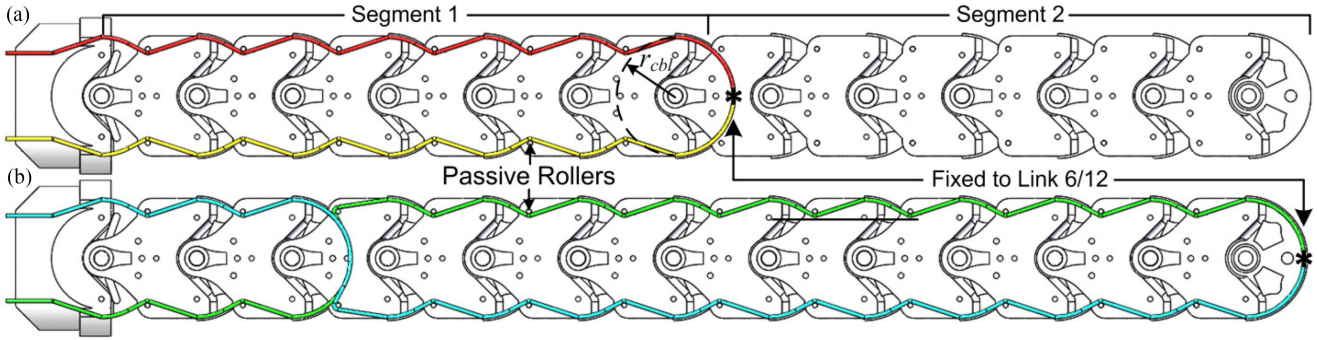
Fig. 3.   R3RT cabling. (a) Segment 1 cable routing. (b) Segment 2 cable routing with S-path arrangement through Segment 1.
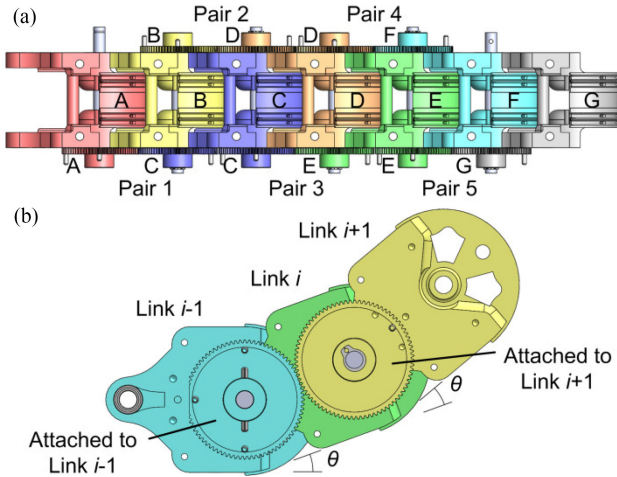

Fig. 4.   R3RT gearing. (a) Single-segment gear arrangement for Links A–G; each gear's color and label indicate the link to which the gear is rigidly attached. (b) Angle constraint from gear pair.

cable path on Links 0–2 and Links 3–5 will extend and shorten the cable path by equal amounts, creating a null space for the Segment 2 cable displacements with respect to Segment 1's motion. However, this assumes that the joint angles along the segment are equal.

To ensure equal joint angles in each segment, the R3RT utilizes five gear pairs mounted along each segment. Each gear pair is mounted on two links with a single link separating them, as shown in Fig. 4(a). For example, in the first gear pair, the first gear (red/A) meshes with the second gear (purple/C) with an intermediate link (yellow/B) between. The gears in each pair also have equal pitch diameters. For the gear pair associated with Links $i-1$, i, and $i+1$, shown in Fig. 4(b), gears are rigidly attached to Links $i-1$ and $i+1$, with Link i in between. If Link $i-1$ is held fixed, Link i will rotate by angle θ relative to Link $i-1$, and Link $i+1$ will rotate by θ relative to Link i. This is done for the five sequential triplets of Links 0–6 (Segment 1) and Links 6–12 (Segment 2) to ensure equal joint angles along each segment.

Although gears are used in the R3RT to implement the joint coupling, other means of rigidly coupling the links' rotations using linkages may also be considered in the future work, such as a scissor mechanism or a crossed four-bar.

IV. SENSING, ACTUATION, AND ELECTRICAL DESIGN

A. Sensing

Two types of joint-space sensing are integrated into the R3RT: angular position (roll-DOF and cable pulleys) and motor speed. Absolute encoders (US Digital MA3) measure the angular position of the hollow shaft (roll-DOF; see Fig. 2) or cable pulleys (segment DOFs). The roll-DOF encoder mounts on the rigid housing and connects to the actuation module using a timing belt. The segment-DOF encoders connect to the cable pulley through the bevel gear (see Fig. 2). Each motor's angular velocity is estimated by its driver using an incremental encoder (US Digital E4T) mounted on its rear shaft (see Fig. 2).

B. Actuation

To enable high-speed motions, the R3RT is actuated by three Maxon 100 W brushless dc motors (ECi 40) operating in closed-loop position control. These motors were chosen to both meet the torque requirements for experiments presented in this paper and to provide an experimental test platform capable of analyzing a variety of future tail structures. Gear reductions were selected to meet the required cable speeds and force estimates for a range of possible robotic tails.

As discussed in Section III-C, two motors control the R3RT segments' bending through antagonistic cables. A 2:1 reduction bevel gear pair drives the pulley, and a gearbox with a 51:1 reduction drives the pinion gear. The pulley radius and the cylindrical cable routing radius r_{cbl} are equal, ensuring equal pulley rotation and segment bending angles.

The third motor controls the R3RT roll-angle using a spur gear coupled to an internal gear with a gear reduction of 3:1 in addition to the 51:1 gearbox. Incorporating the roll motor within the actuation unit reduces the rigid housing envelope at the cost of increased power required to produce roll motion due to the additional inertia. To minimize this effect, the motors are situated close to the roll-DOF's rotation axis.

C. Electrical Design

Fig. 5 shows the R3RT's electrical design. Two Teensy 3.2 ARM microcontrollers (MCUs) control the system in a master–slave configuration. These MCUs communicate over an UART link through the slip ring. The master MCU mounts to the rigid
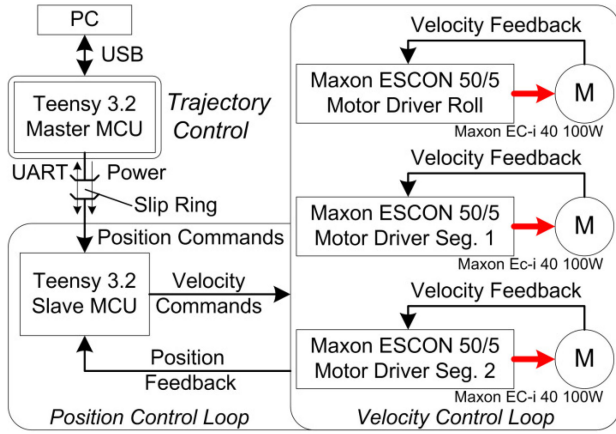
Fig. 5. R3RT electrical design with inner-loop velocity control and outer-loop position control. M denotes motor.
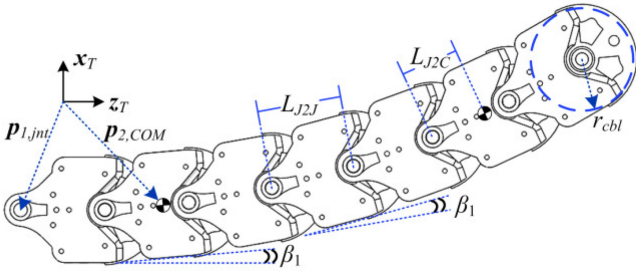

Fig. 6. R3RT kinematic variables.

housing and connects the user PC and slave MCU. The master MCU receives the user's desired joint trajectories, interpolates them into position set points, and sends them to the slave MCU. The master MCU also exercises software control over motor power through a high side MOSFET.

The slave MCU is mounted within the actuation module to ensure robust connections with the sensors and motor drivers. The slave MCU uses a proportional-derivative controller for closed-loop motor position control that generates velocity set points and then sent them to each motor driver (Maxon ESCON 50/5), which operates a closed-loop proportional-integral velocity controller for its motor. The position controller was tuned for near-critical operation on the basis of empirical analysis. The position control loop operates at a control frequency of 450 Hz, which is sufficient for accurate tracking during fast tail trajectories (Section VII).

V. TAIL MODELING

A. Model Overview

The tail model has three inputs—two prescribed cable displacements δ_k for $k \in \{1, 2\}$ and a prescribed roll rotation φ—and five outputs—two segment joint angles β_k (see Fig. 6, wherein each segment's joint angles are equal), two cable tensions T_k, and a roll-DOF torque τ. Internal state variables are β_k, T_k, τ, and ten gear forces $F_{k,j,\text{gear}}$ between gear pair j in Segment k.

The 13 revolute joints lead to 13 equations of motion. If the net moment $M_{i,\text{jnt}}$ is calculated at Joint i, the dot product of $M_{i,\text{jnt}}$ and the Joint i axis unit vector ς_i equals zero, as a revolute joint cannot support a moment about its joint axis. This is defined in (1), where R_i is the Link i orientation matrix and y and z are the y- and z-axis unit vectors. Four loading effects contribute to $M_{i,\text{jnt}}$: gravity $M_{i,\text{grv}}$, inertia $M_{i,\text{inr}}$, gearing $M_{i,\text{gear}}$, and actuation $M_{i,\text{act}}$, shown in (2) and described in greater detail in Section V-C

$$\varsigma_i \cdot M_{i,\text{jnt}} = 0, \quad \varsigma_i = \begin{cases} R_i z, & i = 0 \\ R_i y, & i > 1 \end{cases} \tag{1}$$

$$M_{i,\text{jnt}} = M_{i,\text{inr}} - M_{i,\text{grv}} - M_{i,\text{gear}} - M_{i,\text{act}}. \tag{2}$$

In addition, the model in this section is defined with respect to the tail frame $o x_T y_T z_T$ (frame T) at the tail base. This frame is considered to be stationary in Sections V–VII; a future work will consider the consequences of this frame in motion.

B. Kinematic Model

First, the tail kinematics are defined. Due to the R3RT's cable geometry and gearing, there is a fixed relationship between δ_k and β_k, defined in (3), where r_{cbl} is the cable routing cylinder radius (see Fig. 6). Using these two segment joint angles, (3) also defines a vector of the pitch joint angles θ_i. Using φ and θ_i, R_i is defined in (4), where $R_Z(\varphi)$ and $R_Y(\theta)$ are z-axis and y-axis rotations by angles φ and θ, respectively

$$\beta_k = \delta_k / (6 r_{\text{cbl}}), \quad \theta_i = \begin{cases} \beta_1, & 1 \leq i \leq 6 \\ \beta_2, & 7 \leq i \leq 12 \end{cases} \tag{3}$$

$$R_i = \begin{cases} R_Z(\phi) & i = 0 \\ R_{i-1} R_Y(\theta_i) & i > 0 \end{cases}. \tag{4}$$

Using R_i, the joint positions $p_{i,\text{jnt}}$ and link COM positions $p_{i,\text{COM}}$ may be calculated using 5 and 6, where $p_{0,\text{jnt,lcl}}$ is the position from the frame T origin to Joint 0, $p_{1,\text{jnt,lcl}}$ is the position from Joint 0 to Joint 1, L_{J2J} is the distance between two adjacent pitch joints, $p_{0,\text{COM,lcl}}$ is the position from Joint 1 to the Link 0 COM, and L_{J2C} is the distance between a pitch joint and its COM. In addition, $p_{i,j,J2C}$ in (7) defines the position from Joint i to the Link j COM

$$p_{i,\text{jnt}} = \begin{cases} p_{0,\text{jnt,lcl}} & i = 0 \\ p_{i-1,\text{jnt}} + R_{i-1} p_{1,\text{jnt,lcl}} & i = 1 \\ p_{i-1,\text{jnt}} + L_{J2J} R_{i-1} z & i > 1 \end{cases} \tag{5}$$

$$p_{i,\text{COM}} = \begin{cases} p_{i,\text{jnt}} + R_i p_{0,\text{COM,lcl}} & i = 0 \\ p_{i,\text{jnt}} + L_{J2C} R_i z & i > 0 \end{cases} \tag{6}$$

$$p_{i,j,J2C} = p_{j,\text{COM}} - p_{i,\text{jnt}}. \tag{7}$$

For rotational kinematics, Link i angular velocities ω_i are defined in (8) for the roll ($i = 0$) and pitch ($i > 0$) joints, where
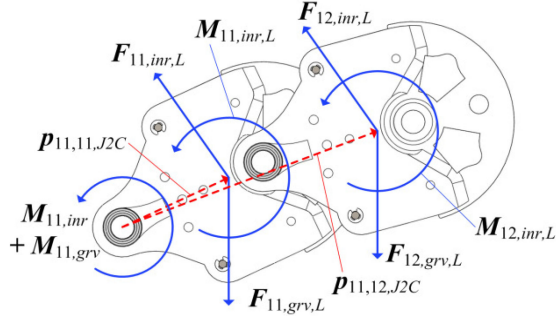
Fig. 7. Free-body diagram of R3RT for calculating F_B and M_B. Loading shown for Links 1, 6, and 12 is representative of the loading for Links 1–12.

$\dot{\varphi}$ denotes the first time derivative of φ:

$$\omega_i = \begin{cases} \dot{\varphi}z & i = 0 \\ \omega_{i-1} + \dot{\theta}R_{i-1}y & i > 0 \end{cases}. \tag{8}$$

C. Dynamic Model

The gravitational moment $M_{i,\mathrm{grv}}$ at Joint i is due to the gravitational forces $F_{j,\mathrm{grv},L}$, acting on Links $j = i$ through $j = 12$. Equation (9) defines $M_{i,\mathrm{grv}}$ and $F_{j,\mathrm{grv},L}$, where $m_{j,L}$ is the Link j mass, g is the gravitational acceleration, $\boldsymbol{\zeta}_{\mathrm{grv}} = -\boldsymbol{x}_T$ is the gravity direction unit vector, and $\tilde{a}b$ denotes $a \times b$. Similar to $M_{i,\mathrm{grv}}$, the inertial moment $M_{i,\mathrm{inr}}$ depends on the Link j inertial force $F_{j,\mathrm{inr},L}$ and inertial moment $M_{j,\mathrm{inr},L}$ of the links "downstream" of the joint. For Joint i, (10) defines the inertial moment generated by Links $j = i$ through $j = 12$, where $I_{j,L,\mathrm{lcl}}$ is the Link j local moment of inertia, $\dot{\omega}_j$ is the Body j angular acceleration, and $\ddot{p}_{j,\mathrm{COM}}$ is the Body j COM acceleration. These moments for Joint $i = 11$ are illustrated in Fig. 7

$$M_{i,\mathrm{grv}} = \sum_{j=i}^{12} \tilde{p}_{i,j,J2C} F_{j,\mathrm{grv},L}, \quad F_{j,\mathrm{grv},L} = m_{j,L}g\boldsymbol{\zeta}_{\mathrm{grv}} \tag{9}$$

$$M_{i,\mathrm{inr}} = \sum_{j=i}^{12} \left(M_{j,\mathrm{inr},L} + \tilde{p}_{i,j,J2C} F_{j,\mathrm{inr},L} \right),$$

$$I_{j,L} = R_j I_{j,L,\mathrm{lcl}} R_j^T$$

$$M_{j,\mathrm{inr},L} = I_{j,L}\dot{\omega}_j + \tilde{\omega}_j I_{j,L}\omega_j, \quad F_{j,\mathrm{inr},L} = m_{j,L}\ddot{p}_{j,\mathrm{COM}}. \tag{10}$$

The force between each gear pair affects the two joints separating those gears. Fig. 8 illustrates the impact of the Link $i + 1$ force on Joints i and $i + 1$. Force $F_{k,j,\mathrm{gear}}$ (from Gear Pair j in Segment k) is mapped into two terms ($M_{i,A,\mathrm{gear}}$ and $M_{i,B,\mathrm{gear}}$) defined in (11) and (12). The *A*-term accounts for the Link $i - 1/i + 1$ gear force pair acting on Joint i, and the *B*-term accounts for the Link $i - 1/i + 1$ gear force pair acting on Joint $i + 1$, assuming that the gear force acts tangential to the gear's
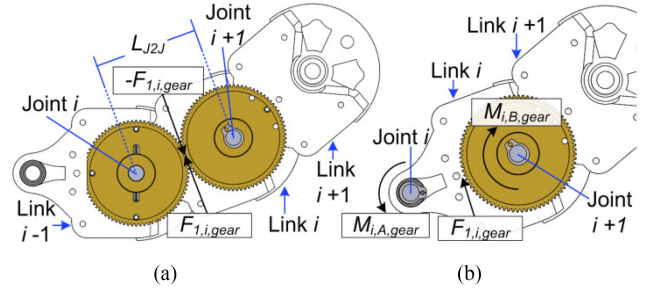

Fig. 8. R3RT gear model. (a) Gear pair illustration. (b) Joint moments due to gear force.
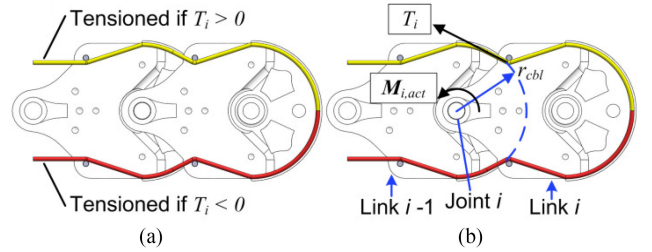

Fig. 9. R3RT cable model. (a) Single-variable tension representation. (b) Joint moment due to cable tension.

diameters. For each joint, (13) defines $M_{i,\mathrm{gear}}$

$$M_{i,A,\mathrm{gear}} = \begin{cases} 0 & i = \{0, 6, 12\} \\ 0.5 L_{J2J} F_{1,i,\mathrm{gear}} & i = \{1, \cdots, 5\} \\ 0.5 L_{J2J} F_{2,i-6,\mathrm{gear}} & i = \{7, \cdots, 11\} \end{cases} \tag{11}$$

$$M_{i,B,\mathrm{gear}} = \begin{cases} 0 & i = \{0, 1, 7\} \\ -0.5 L_{J2J} F_{1,i-1,\mathrm{gear}} & i = \{2, \cdots, 6\} \\ -0.5 L_{J2J} F_{2,i-7,\mathrm{gear}} & i = \{8, \cdots, 12\} \end{cases} \tag{12}$$

$$M_{i,\mathrm{gear}} = (M_{i,A,\mathrm{gear}} + M_{i,B,\mathrm{gear}}) \boldsymbol{\varsigma}_i. \tag{13}$$

Equation (14) formulates the actuation moment $M_{i,\mathrm{act}}$. For Joint 0, the roll-torque acts directly on the joint, but for Joints 1–12, the actuation cabling generates a joint moment

$$M_{i,\mathrm{act}} = \begin{cases} \boldsymbol{\tau}\boldsymbol{\varsigma}_i & i = 0 \\ (T_1 + T_2) r_{\mathrm{cbl}}\boldsymbol{\varsigma}_i & 1 \le i \le 3 \\ (T_1 - T_2) r_{\mathrm{cbl}}\boldsymbol{\varsigma}_i & 4 \le i \le 6 \\ -T_2 r_{\mathrm{cbl}}\boldsymbol{\varsigma}_i & 7 \le i \le 12 \end{cases}. \tag{14}$$

For each antagonistic cable pair, a single real-valued variable T_k represents the nonzero tension in each cable pair. Because cables cannot have negative tension, the antagonistic cables allows for equal and opposite bidirectional tensioning—the "upper" cable tensions when $T_k > 0$, and the "lower" cable tensions when $T_k < 0$ (see Fig. 9). Fig. 9(b) illustrates the mapping of the cable tension into a joint moment: the force vector aligns with the cable between Links $i - 1$ and i and the distance is assumed to be r_{cbl}. In (14), the difference in $M_{i,\mathrm{act}}$ for Joints 1–3 and
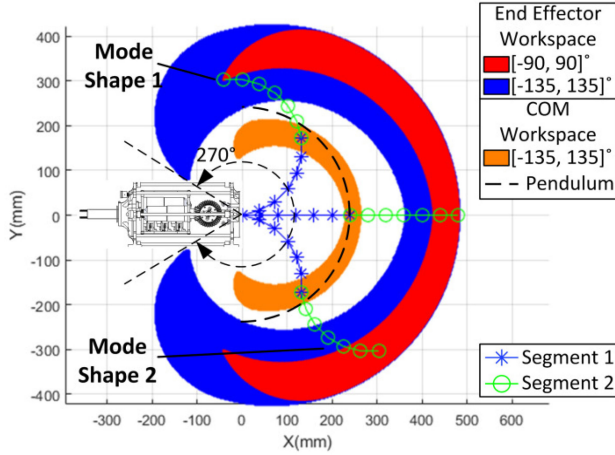
Fig. 10.   Workspace and mode shapes of a 12-link two-segment R3RT.

TABLE II
R3RT SIMULATION PROPERTIES

r_{cbl}	25 mm	L_{J2J}	40 mm	L_{J2C}	32.7 mm
$m_{0,L}$	3.144 kg	$m_{\{1\text{-}12\},L}$	0.0759 kg	$p_{0,jnt,lcl}$	$92.1x$ mm
$p_{1,jnt,lcl}$	$159.24z$ mm	$p_{0,COM,lcl}$	$[-3.52, 0, -7.33]^T$ mm		
$I_{0,B,lcl,xx}$	0.01197 kg-m^2	$I_{0,B,lcl,yy}$	0.01205 kg-m^2	$I_{0,B,lcl,zz}$	0.004202 kg-m^2
$I_{\{1\text{-}12\},B,lcl,xx}$	0.0001868 kg-m^2	$I_{\{1\text{-}12\},B,lcl,yy}$	0.0000813 kg-m^2	$I_{\{1\text{-}12\},B,lcl,zz}$	0.0001626 kg-m^2

4–6 is due to the S-path routing: as the Segment 2 cables routes through Segment 1, their impact on Joints 1–3 and 4–6 is equal and opposite.

Friction will be accomodated in future analyses by scaling the cable tension along the R3RT. Equation (14) assumes the cables route without friction along the R3RT. Due to the segments' kinematic coupling and the use of kinematic inputs to simulate the model, the impact of neglecting friction only manifests in the cable tension T_k calculations.

Using this model, the solutions for τ, T_k, and $F_{k,j,\text{gear}}$ (the model's internal state variables) may be found in the following three steps: calculating T_2 and $F_{2,j,\text{gear}}$ for Segment 2, calculating T_1 and $F_{1,j,\text{gear}}$ for Segment 1 using T_2, and calculating τ.

VI. TAIL ANALYSIS

A. Workspace Analysis

The R3RT can form multicurvature spatial tail configurations for enhanced spatial loading and workspace. Fig. 10 shows the R3RT's two mode shapes: mode shape 1 is a C-shape with the segments bent in parallel, and mode shape 2 is an S-shape with the segments bent in opposition.

The end effector and COM workspaces are the loci of positions the Link 12 tip and COM can reach, respectively. The end effector workspace is computed using the R3RT's forward kinematics (see Section V-B) based on the geometric parameters extracted from the R3RT CAD and prototype (see Figs. 1 and 14), defined in Table II. Fig. 10 shows the R3RT's planar workspaces (end effector and COM) with the roll angle fixed at
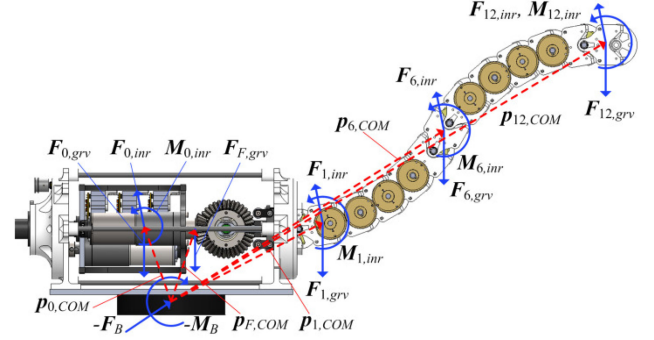

Fig. 11.   Free-body diagram of R3RT for calculating F_B and M_B. Loading shown for Links 1, 6, and 12 is representative of the loading for Links 1–12.

90°. The workspaces are simulated using 300×300 input pairs of the pulley angles (resolution of 0.6° and 0.9° for spool ranges $\pm 90°$ and $\pm 135°$, respectively). The coordinate frame origin is the R3RT Joint 1. The $\pm 135°$ spool rotation range is associated with the maximum R3RT workspace possible without Link 12 contacting the rigid housing.

A robot's COM workspace is defined by its range of motion, mass distribution, link geometry, and the number of independently actuated tail segments. For the R3RT, the COM workspace, with no added tip-mass, is simply the end-effector workspace scaled down as shown in Fig. 10. In a single plane, the R3RT COM workspace spans 190°. The workspace data in Table I for prior robotic tails represents both the end-effector and COM workspaces since the mass is connected to the tip of a pendulum-like structure. However, planar pendulum-like tails' COM workspace is a circular arc (see Fig. 10); for spatial pendulums, this workspace becomes a spherical surface. Comparatively, the R3RT possesses a higher dimensionality end-effector workspace due to its increased articulation and ability to achieve two mode shapes. As a result, the R3RT has significantly greater ability to adjust its COM by changing the distance between the COM and tail base. However, the R3RT COM workspace range in Fig. 10 falls 65° short of [12], but this deficit can be overcome by adding a 450 g tip mass to match the 255° COM workspace and further increase the COM workspace volume.

B. Tail Base Loading

When the R3RT is mounted on a load cell or mobile robot, an internal force F_B and moment M_B acting on the rigid housing are generated, along with equal and opposite loading, F_T and M_T, acting on the load cell or robot. As shown in Fig. 11, the loading F_B and M_B depends on the inertia of the tail's moving links and the gravitational force acting at the tail's links COMs. These calculations are performed with respect to frame $ox_Ty_Tz_T$. As the gear and actuation loading are internal loading effects, they do not contribute to F_B or M_B.

Equations (15) and (16) define F_B and M_B based on Fig. 11, where m_F is the mass of the rigid housing, $F_{F,\text{grv}}$ is the rigid housing's gravitational force, and $p_{F,\text{COM}}$ is the position of the

rigid housing COM relative to the base frame:

$$
\boldsymbol{F}_B = \begin{pmatrix} -\boldsymbol{F}_{F,\mathrm{grv}} \\ +\sum_{i=0}^{n} \left(\boldsymbol{F}_{i,\mathrm{inr},L} - \boldsymbol{F}_{i,\mathrm{grv},L} \right) \end{pmatrix}, \quad \boldsymbol{F}_{F,\mathrm{grv}} = m_F g \boldsymbol{\zeta}_{\mathrm{grv}}
$$
(15)

$$
\boldsymbol{M}_B = \begin{pmatrix} -\tilde{\boldsymbol{p}}_{F,\mathrm{COM}} \boldsymbol{F}_{F,\mathrm{grv}} \\ +\sum_{i=0}^{n} \left(\boldsymbol{M}_{i,\mathrm{inr},L} + \tilde{\boldsymbol{p}}_{i,\mathrm{COM}} \left(\boldsymbol{F}_{i,\mathrm{inr},L} - \boldsymbol{F}_{i,\mathrm{grv},L} \right) \right) \end{pmatrix}.
$$
(16)

C. Tail Loading Profiles

In order to utilize the R3RT's kinematic and dynamic models to simulate the tail base loading, the parameters used to calculate $\boldsymbol{F}_B$ and $\boldsymbol{M}_B$ in (15) and (16) are provided in Table II. These properties match the prototype in Section VII, to allow comparison of the simulated and measured results.

In addition, trajectories of δ_k and φ are required. For δ_k, trajectories of the segment bending angles ψ_k are defined using a sixth-order polynomial and mapped into δ_k (17), where t is the simulation time, t_0 and t_f are the trajectory start and end times, respectively, ψ_0 and ψ_f are the segment angle start and end values, respectively, and $a_{k,i}$ is the segment k ith-order coefficient. The coefficients are found using (18) boundary conditions. A similar process is used to define the roll angle, replacing ψ with φ.

$$
\psi_k = \begin{cases} \sum_{i=0}^{5} a_{k,i} t^i, & t_0 \le t \le t_f \\ \psi_f & t > t_f \end{cases}, \quad \delta_k = r_{\mathrm{cbl}} \psi_k
$$
(17)

$$
\psi_k(t_0) = \psi_0, \quad \dot{\psi}_k(t_0) = 0, \quad \ddot{\psi}_k(t_0) = 0
$$

$$
\psi_k(t_f) = \psi_f, \quad \dot{\psi}_k(t_f) = 0, \quad \ddot{\psi}_k(t_f) = 0.
$$
(18)

Two case studies are considered: dynamic tail bending for fixed roll angles and dynamic tail rolling for fixed bending angles. For both case studies, the tail's static loading when $\varphi = \psi_k = 0$ is subtracted from the calculated loading profile trajectories to emphasize the change in loading that would impact the legged robot on which the tail is mounted.

Fig. 12 illustrates the $\boldsymbol{F}_B$ and $\boldsymbol{M}_B$ profiles for the first case, where $(t_0, t_f) = (0, 0.5)$ s, $(\psi_0, \psi_f) = (0, 90)°$, and $\varphi = \{0, 45, 90\}°$. $F_{B,z}$, due primarily to centripetal acceleration, is invariant to φ since $\boldsymbol{z}_T$ is the roll axis; for $M_{B,z}$, as roll increases, gravity acting over increasing the y-axis distance generates a moment. For $F_{B,x}$ and $F_{B,y}$, as φ increases, the time-varying component of $F_{B,x}$ reallocates to $F_{B,y}$, due to the tail links' centripetal and tangential accelerations. The $M_{B,x}$ and $M_{B,y}$ components are due to the links' angular acceleration moments, the inertial forces moments from the links' linear acceleration, and gravity. Gravity primarily impacts $M_{B,y}$ as the gravitational moment is greatest when $\psi = 0$ and least when $\psi = 90°$. As with force, the roll angle reallocates the inertial component between $M_{B,x}$ and $M_{B,y}$.

Fig. 13 illustrates the loading profiles for the second case, where $(t_0, t_f) = (0, 0.5)$ s, $(\varphi_0, \varphi_f) = (0, 90)°$, $\psi_1 = \{45,$
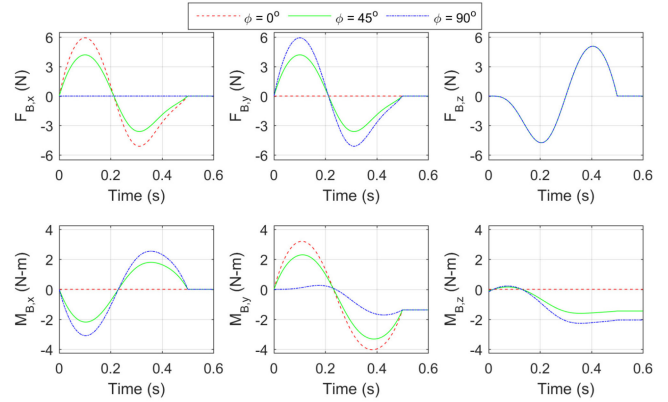

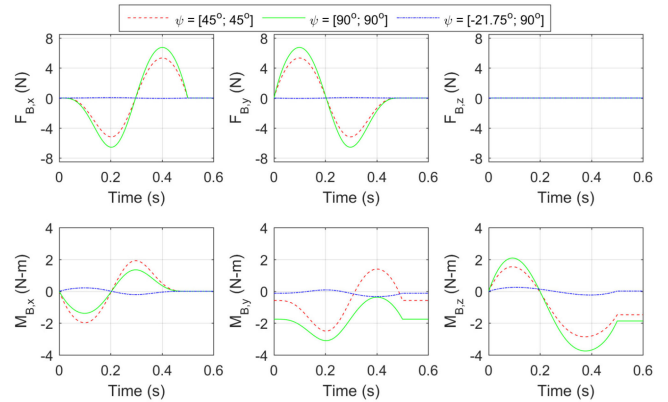Fig. 12. Simulation results: dynamic tail bending loading at fixed roll angles.

Fig. 13. Simulation results: dynamic tail rolling loading at fixed tail bending.

$90, -21.75\}°$, and $\psi_2 = \{45, 90, 90\}°$. The pair $\psi = [-21.75; 90]°$ corresponds to a tail configuration with the tail COM located along the roll axis, similar to a reaction wheel, resulting in zero force variation. However, since the tail is not axisymmetric (there are off-diagonal terms in the tail's inertia tensor), the moment has nonzero $M_{B,x}$, $M_{B,y}$, and $M_{B,z}$.

For the $\psi = \{45, 90\}°$ cases, the tail COM is held at a fixed distance along the z-axis, resulting in zero $F_{B,z}$. The $F_{B,x}$ and $F_{B,y}$ components are due to centripetal and tangential accelerations. However, gravity generates nonzero $M_{B,y}$ and $M_{B,z}$. For $M_{B,y}$, this is due to the reduced tail COM distance from the tail base for $\psi_k = \{45, 90\}°$ compared to $\psi_k = 0°$ (the static loading for $\varphi = \psi_k = 0°$ includes a y-axis moment component). For $M_{B,z}$, as φ increases from $0°$ to $90°$, the y-axis distance between the COM and tail base increases, creating a gravitational moment. For the inertial components of $M_{B,x}$ and $M_{B,y}$, the loading's inertial component magnitude initially increases $(\psi_k = 45°)$ and then decreases $(\psi_k = 90°)$, due to the varying of the z-axis tail COM coordinate and the distance of the tail COM from the z-axis as ψ_k increases. For the inertial component of $M_{B,z}$, the tail's tangential acceleration generates a slight inertial moment secondary to the gravitational change as ψ_k increases.
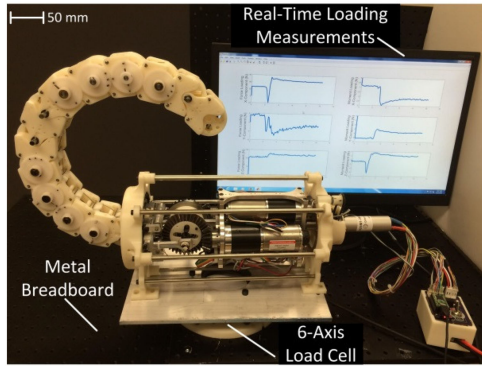
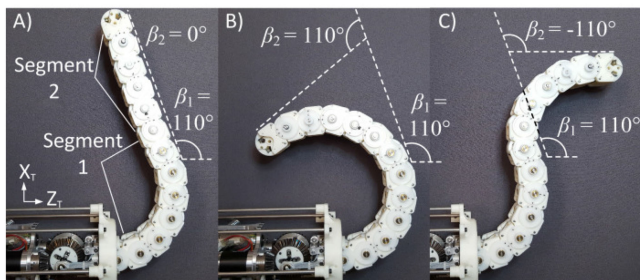Fig. 14. Experimental setup of the R3RT.

Fig. 15. R3RT tail decoupled actuation. (a) Segment 1 bends, while Segment 2 remains fixed. (b) Mode shape 1. (c) Mode shape 2.
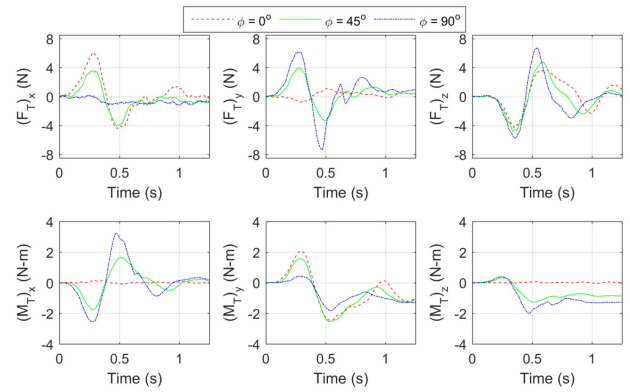

Fig. 16. Experimentally measured loading profiles for fixed-roll experiments.
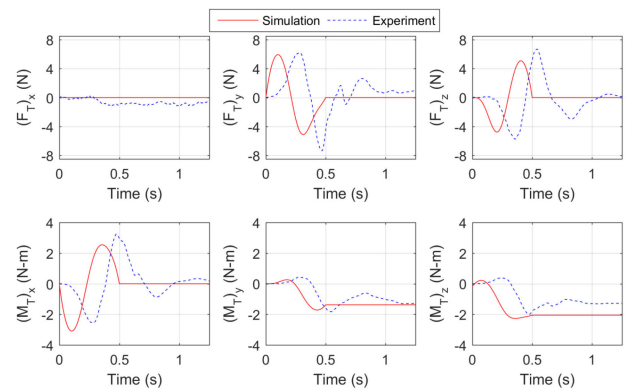
Fig. 17. Comparison of simulation and experimental tail loading results when $\varphi = 90°$.

The loading profiles of Fig. 13 can act over extended time durations due to infinite roll motion, similar to a reaction wheel, because of the slip ring, which is a performance advantage compared to existing tails reviewed in Section II-B.

VII. EXPERIMENTAL PROTOTYPE AND RESULTS

A. Tail Implementation

Fig. 14 shows the R3RT experimental prototype, and Fig. 15 illustrates the tail's decoupled actuation and mode shapes. The tail's links and rigid housing's frames were printed using ABS plastic, and the total tail mass is 4.02 kg. The remaining custom structural components were fabricated from metal (steel shafts, aluminum otherwise). Braided nylon cables (MagicShield) rated for 441 N (100 lbs) actuate the tail; Segment 1 actuation required double routed cable lines to accommodate peak tensions during tail motions. During integration, cable routing was iterated through experiments to minimize friction effects by relieving aggressive cable routing angles about the small sized pins with passive rollers (see Fig. 3).

B. Loading Results

Experiments were performed using a six-axis load cell to measure the tail's ability to generate dynamic loading (see Fig. 14). Sensors were sampled at 400 Hz using a PCI data acquisition card. A moving window mean low-pass filter (width, 50 sample pts) was used to filter out high-frequency sensor noise; sufficient

data was collected before initiating tail motion to uniformly filter the relevant time span.

Tail bending motions with $(t_0, t_f) = (0, 0.5)$ s, $(\psi_0, \psi_f) = (0, 90)°$ and $\varphi = \{0, 45, 90\}°$ (see Section VI-C) were performed to compare measured loading profiles to simulation. Fig. 16 illustrates the measured loading, and Fig. 17 compares the $\varphi = 90°$ results. Each experiment was conducted three times and the results were averaged. From the figure, tail curvature motion is observed to complete in 0.8 s, after which the tail vibrates until it reaches steady-state conditions.

The measured loading exhibits changes similar to the simulated loading (see Fig. 12) as φ varies: the force along the z-axis shows approximate invariance to φ, terminal y- and z-axis gravitational moment loading offsets approximately match simulated results, and the experimental trajectories qualitatively match the simulated trajectories but do not exactly match the idealized smooth contours. The experimental results exhibit similar peak magnitudes and nontrivial lag behind the simulation. This is primarily due to the feedback-based velocity controller used to generate the tail motor inputs. As discussed in Section VIII, controllers utilizing feedback terms that ensure stability in parallel with feedforward terms that enable rapid response and reduce lag will be studied in the future work to improve this shortcoming.

TABLE III
MEAN MEASURED LOADING PROFILES OF ARTICULATED VERSUS
SINGLE-BODY RIGID PENDULUM TAIL IN CONSTANT TENSION EXPERIMENTS

Cable Tension	Tail Structure	$F_{B,z}$ (N)	$F_{B,y}$ (N)	$M_{B,x}$ (Nm)
60N	Articulated	-2.1	-1.06	-0.48
	Pendulum	-1.89	-2.83	-0.27
110N	Articulated	-6.7	-1.78	-0.93
	Pendulum	-6.36	-3.19	-0.72

C. Comparing Articulated and Pendulum Inertial Loading

Experiments were performed to compare the inertial loading profiles of an articulated tail structure to a single-body rigid pendulum, which was analyzed in simulation in [1]. To facilitate this comparison, the 12-link R3RT tail structure was reconfigured in the following two ways: first, as an articulated single-DOF tail segment with equal joint angles constrained by 11 gear pairs, and second, as a single-body rigid pendulum with immobilized gears capable rotating about its revolute Joint 1. For consistency of power input and range of motion, both tail configurations were actuated by prescribing a constant input cable tension as the tail rotated through its trajectory of equal cable displacement at a fixed roll angle of 90°, which produced a planar horizontal tail motion unaffected by gravity. This resulted in COM angular displacement ranges of 104° and 180° for the articulated and pendulum tails, respectively.

Loading profiles for both tails were generated with constant cable tensions of 60 and 110 N. These motions were performed ten times for each tail structure with measured results averaged. The time spans to complete motions were slower for the articulated tail (60 N, 0.63 s; 110 N, 0.48 s) compared to the pendulum-like tail (60 N, 0.58 s; 110 N, 0.42 s). The articulated tail motions likely require slightly longer time spans due to cable friction along the structure. Table III presents the mean measured inertial loading. For equivalent input cable displacements and constant cable tensions, the articulated tail provides, on average, a 53% increase in base moment $M_{B,x}$, a 52% reduction in $F_{B,y}$, and an 8% increase in $F_{B,z}$. Since the primary function of a robotic tail is to generate desired moments about a specific axis, such a significant improvement in average moment over the duration correlates to greater tail efficacy in achieving maneuvering or stabilization goals, as will be demonstrated in the future work.

These experiments highlight the enhanced inertial loading that tail articulation can provide about its attachment point for applications like adjusting attitude, dynamically self-righting, or maneuvering, as discussed in [20] and corroborated in [1].

D. Repeatability Results

In addition to analyzing the R3RT's inertial loading, the cable-driven mechanism's accuracy and repeatability were also analyzed. This analysis is critical for tasks involving precise COM adjustments due to the mechanism's need to effectively transition tension between a segment's cable pair without impacting the robot's configuration as it moves.
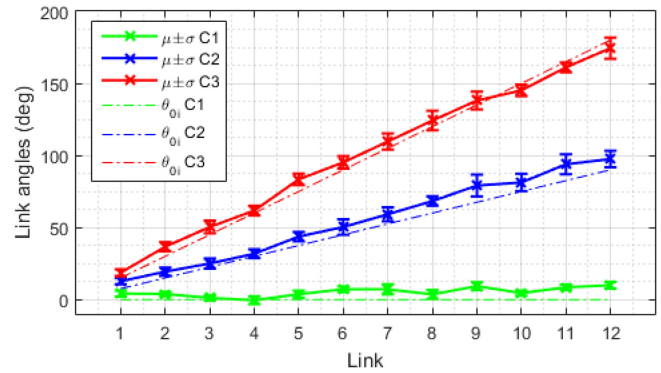

Fig. 18. Repeatability experimental results showing mean and standard deviation of measured link angles and deviations from expected values θ_{0i}.

The R3RT was cycled between the tail curvatures C1, C2, and C3 associated with pulley angles of 0°, 45°, and 90° at a fixed roll angle of 90°. Individual joint angles were measured by a Point Grey Blackfly camera (BFLY-U3-13S2M-CS) mounted orthogonally to the R3RT's bending plane. Image processing was used to measure the relative link orientations with respect to the R3RT's roll axis using 150 frames for each configuration over five consecutive cycles. Fig. 18 shows the expected and measured link angles for the 12 joints for the three configurations in the form of an error plot showing the measured mean μ and standard deviation σ.

For the C1 angles, slight offsets are observed from the home configuration (max. offset: segment 1, 4.1°; segment 2, 6.1°). These offsets exist due to discrete meshing of the gear teeth that prevent a perfectly straight home configuration during assembly. For configurations C2 and C3, the links furthest from the base showed the largest error and repeatability of up to ±10.5° and ±6.7°. The primary factors that introduce these inconsistencies are gear backlash and slight cable slack. As each gear pair rotates, slight variations due to the tooth geometry modify the relative angle between the links. For the cable tensions, a slight slack on one cable in each pair is needed to prevent the mechanism from locking up during operation. Lock ups result from highly tensioned segment cables that prevent rotation in either direction and introduce a hysteresis-type effect in the links' responses to pulley inputs.

VIII. QUADRUPED MANEUVERING

This section analyzes how the R3RT's inertial loading can perform quadruped yaw-angle maneuvering. This is similar to [18], but the foot contact forces, including friction, are neglected to emulate lizard [6], [18], cheetah [20], and kangaroo [10], [13] tail usages during the airborne phases of gaits.

A. Quad and Tail Model

Fig. 19 illustrates the integrated quadruped/tail concept. The R3RT is mounted on-board a four-legged robot capable of running using single-DOF legs currently under development that utilize high-power Maxon brushless dc motors to propel the robot. The tail aids in stabilization and maneuvering.
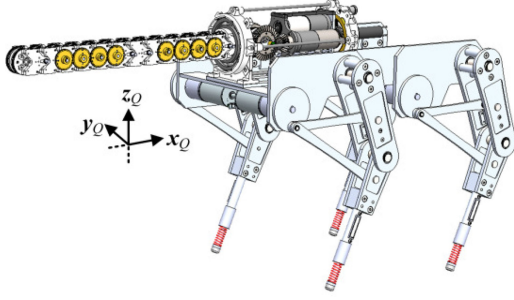
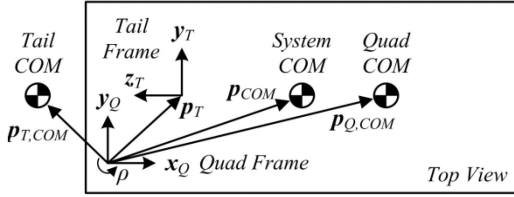Fig. 19.   Integrated quadruped and tail concept design.

Fig. 20.   Quadruped with tail model kinematic variables.

To model the yaw-angle dynamic behavior of this system, a kinematic model is needed to connect the quadruped and tail subsystems. Fig. 20 illustrates the kinematic variables relative to the quadruped frame $o x_Q y_Q z_Q$, where ρ is the quadruped yaw angle, p_T is the tail frame position, $p_{T,\text{COM}}$ is the tail COM position, $p_{Q,\text{COM}}$ is the quadruped COM position, and p_{COM} is the system COM position. Both p_T and $p_{Q,\text{COM}}$ are fixed, and $p_{T,\text{COM}}$ is calculated using (19), where m_F is the tail's rigid housing mass, $p_{F,\text{COM}}$ is the rigid housing COM position relative to the tail frame, m_T is the total tail mass (20), and R_{QT} is the tail frame orientation relative to the quadruped frame (20). Using $p_{T,\text{COM}}$, p_{COM} is calculated using (21), where m_Q is the quadruped mass, along with p_{C2T}, the position from the system COM to the tail base frame

$$p_{T,\text{COM}} = p_T + R_{QT}\left(\frac{m_F}{m_T}p_{F,\text{COM}} + \sum_{i=0}^{n}\frac{m_{i,L}}{m_T}p_{i,\text{COM}}\right) \tag{19}$$

$$R_{QT} = R_Y\left(-90°\right), m_T = m_F + \sum_{i=0}^{n}m_{i,L} \tag{20}$$

$$p_{\text{COM}} = \left(m_Q p_{Q,\text{COM}} + m_T p_{T,\text{COM}}\right)/\left(m_Q + m_T\right)$$
$$p_{C2T} = p_{T,\text{COM}} - p_{\text{COM}}. \tag{21}$$

A dynamic model for the system's planar yaw rotation ρ is defined in (22) based on [1], where I is the effective system inertia at its COM (calculated using the parallel axis theorem based on the quadruped mass m_Q and inertia I_Q, fixed link mass m_F and inertia I_F, and link mass $m_{i,L}$ and inertia $I_{i,L}$), ω is the quadruped angular velocity (23), and F_T and M_T are the force and moment applied on the quadruped by the tail, respectively (23, equal to and opposite of F_B and M_B). The z-component

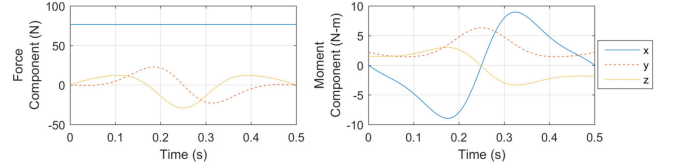| m_F	2.217 kg	m_Q	16.252 kg	$p_{F,COM}$	[66.56; 0; 13.98] mm
p_T	[157.5; 0; 15] mm			$p_{Q,COM}$	[295.28; 0; -34.08] mm
$I_{O,xx}$	0.50856 kg-m²	$I_{O,yy}$	0.67366 kg-m²	$I_{O,zz}$	0.95609 kg-m²
$I_{O,xy}$	-0.00003 kg-m²	$I_{O,yz}$	-0.00001 kg-m²	$I_{O,xz}$	-0.04440 kg-m²
$I_{F,xx}$	0.041318 kg-m²	$I_{F,yy}$	0.042730 kg-m²	$I_{F,zz}$	0.006878 kg-m²
$I_{F,xy}$	-0.000017 kg-m²	$I_{F,yz}$	0.000371 kg-m²	$I_{F,xz}$	0.000040 kg-m²

Fig. 21.   Tail loading F_B and M_B applied to quadruped by tail.

equation of (22) is used for the yaw-angle dynamics

$$I\dot{\omega} + \tilde{\omega}I\omega = M_T + \tilde{p}_{C2T}F_T \tag{22}$$

$$\omega = \begin{bmatrix} 0 & 0 & \dot{\rho}\end{bmatrix}^T, \, F_T = -R_{QT}F_B, \, M_T = -R_{QT}M_B \cdot \tag{23}$$

To calculate I in (24) using the tensor generalization of the parallel axis theorem, the tail's net inertia I_T is needed, defined in (25), where I_F is the tail-frame inertia of the rigid housing at its COM and E_3 is the 3-by-3 identity matrix

$$I = I_Q + m_Q \bar{p}_{C2Q} + I_T + m_T \bar{p}_{C2T} \tag{24}$$

$$I_{T,\text{lcl}} = I_F + m_F \bar{p}_{TC2F} + \sum_{i=0}^{n}\left(I_{i,L} + m_{i,L}\bar{p}_{i,TC2C}\right)$$

$$\bar{p} = \left(p^T p\right)E_3 - pp^T, \, I_T = R_{QT}I_{T,\text{lcl}}R_{QT}^T. \tag{25}$$

Table IV provides the simulation parameters extracted from the system CAD model shown in Fig. 19 used in this analysis, along with the tail properties in Section VI. The tail gravity unit vector ζ_{grv} for this section is defined in the following equation:

$$\zeta_{\text{grv}} = -R_{QT}^T x. \tag{26}$$

B. Simulation Results

Using this model, the impact of the tail's loading on quadruped rotation is considered. Fig. 20 shows the loading profiles for a tail motion at fixed roll $\varphi = 90°$ with ψ_k varying from $-90°$ to $90°$ in 0.5 s using the polynomial trajectory interpolation in (17) and (18). This loading was applied to a Simulink model implementing the z-component of (22), and a net rotation of 12.77° was calculated based on the $\ddot{\rho}$ trajectory generated by the tail loading and is shown in Fig. 21.

Fig. 22 also shows the contributions to $\ddot{\rho}$ due to the x-component of M_B and the y- and z-components of F_B (the other three loading components did not contribute to $\ddot{\rho}$). The moment x-component contributes the most to the loading and subsequent rotation (10.71°), followed by the force y-component
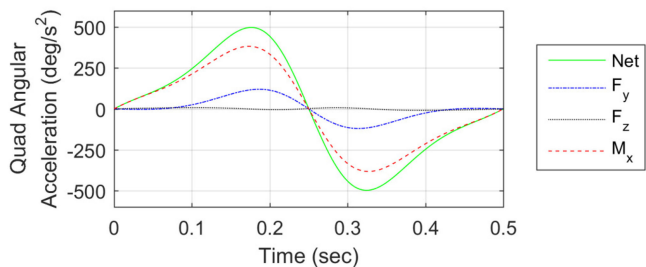
Fig. 22. Net quadruped yaw acceleration profile and contributions from $F_{B,y}$, $F_{B,z}$, and $M_{B,x}$.

(1.80°), and the force z-component (0.26°). This is due primarily to the relatively small position vector $\boldsymbol{p}_{C2T}$, compared to the tail COM position relative to the tail base frame. Hence, the tail inertial forces that contribute to $\boldsymbol{M}_B$ over the position vector from the tail base to the tail COM overshadow the $\boldsymbol{F}_B$ contributions to $\ddot{\rho}$.

IX. CONCLUSION AND FUTURE WORK

This paper focused on a novel robotic system design capable of generating spatial dynamic loading with respect to its base. The R3RT is a serpentine structure capable of continuously rolling with respect to its fixed housing, as well as bending two independently actuated segments using two pairs of antagonistic cables each driven by a single motor. A prototype was integrated to compare measured loading generated by the robot to the loading predicted by the R3RT's dynamic model. This experimentally demonstrated the loading benefits of an articulated structure over a pendulum-like structure and the mechanism's repeatability.

A key takeaway is the need for a more advanced controller for implementing the desired R3RT motion. The experiments in Section VII-B only use motor feedback to calculate motor torque; in the future, feedforward contributions are needed to account for the torque necessary to drive the robot at a desired speed with feedback contributions ensuring tail stability.

The future work will focus on the task planning and control considerations necessary for using the R3RT system design as a tail. For task planning, tail trajectories capable of generating significant spatial loading in a desired direction (yaw, pitch, or roll) that minimize the secondary loading in the other directions will be analyzed to ensure this secondary loading does not destabilize the legged robot. For control, outer-loop controllers implementing these trajectories in light of the legged robot's feedback will be formulated and inner-loop controllers designed to calculate motor torque inputs based on the desired R3RT trajectory (feedforward contribution) and the R3RT's measured sensor data (feedback contribution). In terms of the model formulations, a means of estimating friction along the R3RT will be incorporated into the model to more accurately estimate the additional torque the motors will need to provide to generate the desired tail motion. In addition, an enhanced experimental setup will be developed to enable hardware-in-the-loop simulations of the prototype tail in conjunction with a simulated legged platform, using the six-axis load cell to measure the tail's real-time dynamic loading. Finally, further design iterations for the R3RT will be performed to explore alternative means of implementing the mechanism, miniaturize the tail links for metal fabrication, and investigate methods to reduce cable routing friction.

REFERENCES

[1] W. S. Rone and P. Ben-Tzvi, "Dynamic modeling and simulation of a yaw-angle quadruped maneuvering with a robotic tail," *J. Dyn. Syst. Meas. Control*, vol. 138, no. 8, 2016, Art. no. 084502.

[2] W. Saab and P. Ben-Tzvi, "Design and analysis of a discrete modular serpentine tail," in *Proc. ASME Int. Design Eng. Tech. Conf. Comput. Inf. Eng. Conf.*, 2016, Art. no. 59387.

[3] W. S. Rone, P. Ben-Tzvi, "Maneuvering and stabilizing control of a quadrupedal robot using a serpentine robotic tail," in *Proc. IEEE Conf. Control Technol. Appl.*, 2017, pp. 1763–1768.

[4] S.-H. Lee and A. Goswami, "Reaction mass pendulum (RMP): An explicit model for centroidal angular momentum of humanoid robots," in *Proc. IEEE Int. Conf. Robot. Autom.*, 2017, pp. 4667–4672.

[5] K. Machairas and E. Papadopoulos, "On quadruped attitude dynamics and control using reaction wheels and tails," in *Proc. Eur. Control Conf.*, 2015, pp. 753–758.

[6] T. Libby, M. Johnson, Aaron, E. Chang-Siu, R. J. Full, and D. E. Koditschek, "Comparative design, scaling, and control of appendages for inertial reorientation," *IEEE Trans. Robot.*, vol. 32, no. 6, pp. 1380–1398, Dec. 2016.

[7] A. Patel and E. Boje, "On the conical motion of a two-degree-of-freedom tail inspired by the cheetah," *IEEE Trans. Robot.*, vol. 31, no. 6, pp. 1555–1560, Dec. 2015.

[8] A. Patel and M. Braae, "Rapid acceleration and braking: Inspiration from the cheetah's tail," in *Proc. IEEE Int. Conf. Robot. Autom.*, 2014, pp. 793–799.

[9] A. Patel and M. Braae, "Rapid turning at high-speed: Inspirations from the cheetah's tail," in *Proc. IEEE/RSJ Int. Conf. Int. Robots Syst.*, 2013, pp. 5506–5511.

[10] G.-H. Liu, H.-Y. Lin, H.-Y. Lin, S.-T. Chen, and P.-C. Lin, "A bio-inspired hopping kangaroo robot with an active tail," *J. Bionic Eng.*, vol. 11, no. 4, pp. 541–555, 2014.

[11] V. Kopman, J. Laut, F. Acquaviva, A. Rizzo, and M. Porfiri, "Dynamic modeling of a robotic fish propelled by a compliant tail," *IEEE J. Ocean. Eng.*, vol. 40, no. 1, pp. 209–221, Jan. 2015.

[12] E. Chang-Siu, T. Libby, M. Tomizuka, and R. J. Full, "A lizard-inspired active tail enables rapid maneuvers and dynamic stabilization in a terrestrial robot," in *Proc. IEEE/RSJ Int. Conf. Int. Robots Syst.*, 2011, pp. 1887–1894.

[13] G. He and Z. Geng, "Exponentially stabilizing an one-legged hopping robot with non-SLIP model in flight phase," *Mechatronics*, vol. 19, no. 3, pp. 364–374, 2009.

[14] N. J. Kohut, D. W. Haldane, D. Zarrouk, and R. S. Fearing, "Effect of inertial tail on yaw rate of 45 gram legged robot," in *Proc. Int. Conf. Climbing Walking Robots Support Technol. Mobile Mach.*, 2012, pp. 157–164.

[15] W. R. Provancher, S. I. Jensen-Segal, and M. A. Fehlberg, "ROCR: An energy-efficient dynamic wall-climbing robot," *IEEE/ASME Trans. Mechatronics*, vol. 16, no. 5, pp. 897–906, Oct. 2011.

[16] F. J. Berenguer and F. M. Monasterio-Huelin, "Zappa, a quasi-passive biped walking robot with a tail: Modeling, behavior, and kinematic estimation using accelerometers," *IEEE Trans. Ind. Electron.*, vol. 55, no. 9, pp. 3281–3289, Sep. 2008.

[17] A. Mutka, M. Orsag, and Z. Kovacic, "Stabilizing a quadruped robot locomotion using a two degree of freedom tail," in *Proc. 21st Mediterranean Conf. Control Autom.*, 2013, pp. 1336–1342.

[18] E. Chang-Siu, T. Libby, M. Brown, R. J. Full, and M. Tomizuka, "A nonlinear feedback controller for aerial self-righting by a tailed robot," in *Proc. IEEE Int. Conf. Robot. Autom.*, 2013, pp. 32–39.

[19] A. De and D. E. Koditschek, "Parallel composition of templates for tail-energized planar hopping," in *Proc. Int. Conf. Robot. Autom.*, 2015, pp. 4562–4569.

[20] R. Briggs, J. Lee, M. Haberland, and S. Kim, "Tails in biomimetic design: Analysis, simulation, and experiment," in *Proc. IEEE/RSJ Int. Conf. Int. Robots Syst.*, 2012, pp. 1473–1480.

[21] W. S. Rone and P. Ben-Tzvi, "Continuum robotic tail loading analysis for mobile robot stabilization and maneuvering," in *Proc. ASME Int. Design Eng. Technical Conf. Comput. Inf. Eng. Conf.*, 2014, Art. no. 34678.

[22] P. K. Singh and C. M. Krishna, "Continuum arm robotic manipulator: A review," *Universal J. Mech. Eng.*, vol. 2, no. 6, pp. 193–198, 2014.

[23] S. Kim, C. Laschi, and B. Trimmer, "Soft robotics: A bioinspired evolution in robotics," *Trends Biotechnol.*, vol. 31, no. 5, pp. 287–294, 2013.

[24] Z. Li, R. Du, H. Yu, and H. Ren, "Statics modeling of an underactuated wire-driven flexible robotic arm," in *Proc. IEEE RAS/EMBS Int. Conf. Biomed. Robot. Biomechatron.*, 2014, pp. 326–331.

[25] J. W. Suh, K. Y. Kim, J. W. Jeong, and J. J. Lee, "Design considerations for a hyper-redundant pulleyless rolling joint with elastic fixtures," *IEEE/ASME Trans. Mechatronics*, vol. 20, no. 6, pp. 2841–2852, Dec. 2015.

[26] L.-R. Lin and H.-P. Huang, "NTU hand: A new design of dexterous hands," *J. Mech. Des.*, vol. 120, no. 2, pp. 282–292, 1998.

[27] T. Okada, "Object-handling system for manual industry," *IEEE Trans. Syst., Man, Cybern.*, vol. 9, no. 2, pp. 79–89, Feb. 1979.

[28] P. J. Kyberd, C. Light, P. H. Chappell, J. M. Nightingale, D. Whatley, and M. Evans, "The design of anthropomorphic prosthetic hands: A study of the Southampton hand," *Robotica*, vol. 19, no. 6, pp. 593–600, 2001.

[29] S. Hirose and Y. Umetani, "The development of soft gripper for the versatile robot hand," *Mech. Mach. Theory*, vol. 13, no. 3, pp. 351–359, 1978.

[30] M. G. Catalano, G. Grioli, E. Farnioli, A. Serio, C. Piazza, and A. Bicchi, "Adaptive synergies for the design and control of the Pisa/IIT SoftHand," *Int. J. Robot. Res.*, vol. 33, no. 5, pp. 768–782, 2014.

[31] G. Palli, *Model and Control of Tendon Actuated Robots*. Bologna, Italy: Univ. Bologna, 2006.

William S. Rone, Jr. received the B.S. and Ph.D. degrees in mechanical engineering from The George Washington University, Washington, DC, USA and Virginia Tech, Blacksburg, VA, USA, in 2010 and 2017, respectively.

He is currently a Mechanical Engineer with the United States Air Force, Eglin AFB, FL, USA, focusing on thermal analysis.

Anil Kumar (S'15–M'18) received the B.Tech. degree in electrical engineering from the Indian Institute of Technology (IIT) Roorkee, Roorkee, Uttarakhand, India and the Ph.D. degree in mechanical engineering from Virginia Tech, Blacksburg, VA, USA, in 2010 and 2018, respectively.

He is currently a Senior Engineer with GM Cruise, San Francisco, CA, USA. He has previously served as a Research Fellow in Biomedical Instrumentation Lab, IIT Roorkee. His research interests include machine learning, computer vision, mechatronics design, signal and image processing, autonomous robotics, and instrumentation design.

Pinhas Ben-Tzvi (S'02–M'08–SM'12) received the B.S. degree (summa cum laude) in mechanical engineering from the Technion—Israel Institute of Technology, Haifa, Israel, in 2000 and the M.S. and Ph.D. degrees in mechanical engineering from the University of Toronto, Toronto, ON, Canada, in 2004 and 2008.

He is currently an Associate Professor of mechanical engineering and electrical and computer engineering and the Founding Director of the Robotics and Mechatronics Laboratory, Virginia Tech, Blacksburg, VA, USA. His research interests include robotics and intelligent autonomous systems, mechatronics, human–robot interactions, dynamic systems and control, mechanism design and system integration, and novel sensing and actuation.

Dr. Ben-Tzvi was the recipient of the 2018 Virginia Tech Faculty Fellow Award, as well as several other honors and awards. He is a Technical Editor of the IEEE/ASME Transactions on Mechatronics, an Associate Editor of *ASME Journal of Mechanisms and Robotics*, an Associate Editor for *IEEE Robotics and Automation Magazine*, and an Associate Editor of the *International Journal of Control, Automation and Systems*. He has served as an Associate Editor for IEEE International Conference on Robotics and Automation from 2013 to 2018. He is a Member of the American Society of Mechanical Engineers.

Wael Saab received the B.S. and Ph.D. degrees in mechanical engineering from the American University of Beirut, Beirut, Lebanon and Virginia Tech, Blacksburg, VA, USA, in 2012 and 2018, respectively.

He is currently a Senior Research and Development Engineer with the SoftWear Automation, Inc., developing custom automated systems in the garment manufacturing industry.